IEEE Access
Multidisciplinary ⋮ Rapid Review ⋮ Open Access Journal

Received October 25, 2020, accepted November 15, 2020, date of publication November 17, 2020,
date of current version December 1, 2020.

Digital Object Identifier 10.1109/ACCESS.2020.3038816

Navigation of Unmanned Surface Vehicles Using Underwater Geophysical Sensing

JONGDAE JUNG, (Member, IEEE), JEONGHONG PARK, (Member, IEEE), JINWOO CHOI, (Member, IEEE), AND HYUN-TAEK CHOI, (Member, IEEE)
Korea Research Institute of Ships and Ocean Engineering, Daejeon 34103, South Korea

Corresponding author: Jongdae Jung (jdjung@kriso.re.kr)

This work was supported by a grant from the Endowment Project (Development of Core Technology for Cooperative Navigation of Multiple Marine Robots and Underwater Wireless Cognitive Network) funded by the Korea Research Institute of Ships and Ocean Engineering under Grant PES3560.

ABSTRACT Underwater geophysical properties can provide useful information for surface navigation, particularly in situations where a global navigation satellite system is unavailable. Unmanned surface vehicles (USVs) equipped with geophysical sensors can measure certain types of underwater properties related to Earth geophysics. For example, multibeam echosounders can obtain an array of sonar ranges for underwater terrains, and magnetometers can measure geomagnetic vector fields. These measurements can be used to track vehicle poses if pre-surveyed geophysical maps are provided. This paper proposes geophysical navigation of USVs using a multibeam sonar and magnetometer. The navigation algorithm is implemented within a particle filter framework, and we designed observation models for each geophysical sensor. To avoid the particle impoverishment problem of the conventional terrain based navigation, a terrain roughness measure is employed to modify the weight update and resampling steps of the standard particle filter framework. We conducted field experiments in an inland water environment using the designed surface vehicle, and validated enhanced tracking performance of the proposed methods by comparing the methods with conventional approaches.

INDEX TERMS Geophysical navigation, magnetometer, multibeam echosounder, particle filter, unmanned surface vehicle.

I. INTRODUCTION

The global navigation satellite system (GNSS) is the most common solution that marine surface vehicles depend on to obtain position and heading information in real time. However, it is necessary to prepare for situations where the GNSS is unavailable. For example, during military operations, there is a strong possibility of GNSS jamming or spoofing [1]–[3], or malfunctions of the receiver antenna caused by physical attacks.

Therefore, additional navigation sources are necessary as backup to existing GNSS. Several approaches can be adopted for this purpose. One approach is to utilize existing maritime radio infrastructure as navigation beacons. Unlike weak and vulnerable GNSS signals, maritime radio signals are strong and robust to interference. Examples of these techniques include enhanced long-range navigation (eLoran) [4] and ranging mode (R-Mode) [5]. However, these systems use low-frequency radio ranging and can lead to highly coarse positioning (with accuracy larger than 80 m for eLoran [6] and 50 m for R-MODE [7]) depending on the environment. In addition, the vehicle should be equipped with additional maritime radio signal receivers.

Another approach is to perform dead-reckoning (DR) by onboard proprioceptive sensors such as inertial measurement units (IMUs) and Doppler velocity logs (DVLs). IMUs can measure vehicle linear acceleration and angular velocity in a body-fixed frame, DVLs can measure linear velocity. These signals can be integrated to obtain the three-dimensional (3D) position and orientation of the vehicle [8], [9]. However, DR has the problem of accumulating errors due to sensor noise and biases. Moreover, DVL measurement accuracy is severely degraded with inclined or irregular underwater floors. The third approach is to exploit the map of the environment surrounding the ego vehicle. Any type of properties of the environment that helps vehicle positioning can be utilized

The associate editor coordinating the review of this manuscript and approving it for publication was Sabu M Thampi.

and encoded into maps. If the maps are initially known or provided by operators, the problem becomes a localization or positioning task. If the maps are unknown, then a simultaneous localization and mapping problem must be solved [10]. In this work, we assumed that a certain type of map of the target operation area is constructed before the vehicle starts its mission. For example, if the vehicle operates near bridges, positions and cross-section shapes of the columns can be encoded into a map and utilized for navigation with onboard sensors such as light detection and ranging (LiDAR) or optical cameras [11]. Radar installations and coastline maps can also be used in a similar manner [12] if the vehicle operates near coastlines. Evidently, navigation using these types of maps is restricted to the areas having either bridges or coastlines. In this paper, we propose an unmanned surface vehicle (USV) system navigation that utilizes sensing of underwater geophysical properties, or geophysical navigation (GN). Two types of underwater properties are examined: underwater terrain and geomagnetic fields. The advantages of using these properties in navigation include 1) omnipresence of the signal sources (i.e. terrain and geomagnetic fields) over all water surfaces and 2) low variability between the observed signals acquired at the same position during a long period, or repeatability of observations in the temporal domain.

Multibeam sonar sensors such as the multibeam echosounder (MBES) can obtain an array of sonar ranges with every single sonar transmission and acquire a 2D profile of the underwater terrain, which is considerably more efficient than the single-beam echosounder. The acquired terrain profile can then be matched with existing terrain maps to infer navigation information. This technique, called terrain-based navigation (TBN), is effective in areas with rich terrain features [13]–[16]. However, in areas with sparse terrain features, sonar observations should be used in a selective manner to improve the performance of the tracking filter; otherwise, a local minimum or divergence may occur [17]. In this paper, we propose the use of a terrain roughness measure in the implementation of a particle filter-based TBN algorithm. In particular, the proposed approach attempts to resolve the particle impoverishment problem by modifying the weight update and resampling steps.

The other geophysical property used in the proposed navigation algorithm is the geomagnetic field. A USV is equipped with high-precision underwater magnetometers that can measure the 3D vector or scalar strength of the Earth's magnetic field. Because the Earth's magnetic field is affected by soft and hard iron distortions from the vehicle's metallic body frame and electromagnetic devices such as thrusters, a dedicated calibration procedure is required for the use of magnetometers [18]–[20]. Calibrated magnetic field measurements can then be used as additional navigation features that can enhance the conventional TBN algorithm [21].

In this paper, the construction of geophysical maps is explained in Section II. The design of the GN filter is described in Section III. The field experiment and its results are presented in Section IV, and the conclusions are summarized in Section V.

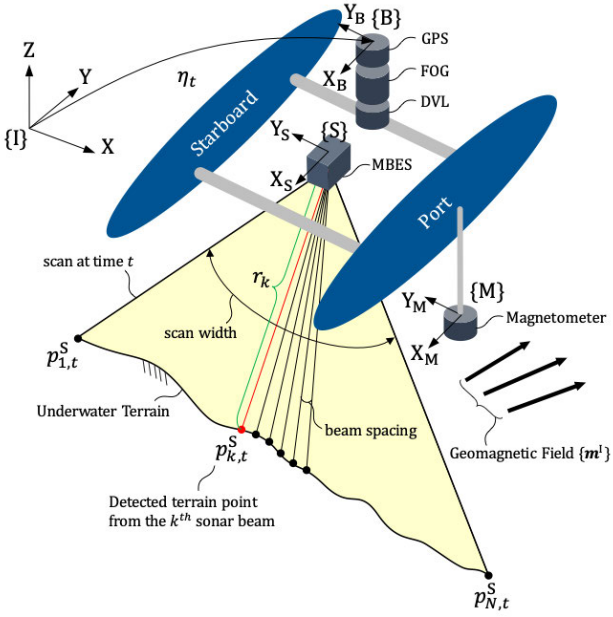

FIGURE 1. Geophysical sensing by MBES and magnetometer installed on a USV.

II. GEOPHYSICAL MAPPING

The first task in geophysical navigation is to obtain reliable geophysical maps. In this work, two types of geophysical properties are exploited: underwater terrains and geomagnetic fields. Bathymetric and geomagnetic maps have already been explored over many years and are now publicly available. For example, the GEBCO grid [22] provides an interpolated grid of bathymetry measurements taken over much of the world's ocean floors. However, this grid generally has low resolution (up to several kilometers), and only certain parts of the ocean floors are mapped with higher resolution. For the geomagnetic field maps, empirical models such as the World Magnetic Model (WMM) [23] and International Geomagnetic Reference Field (IGRF) [24] provide information about the Earth's magnetic field but with updates only every 5 years. Therefore, in this study, we built a high-resolution and up-to-date terrain and geomagnetic maps to guarantee better navigation performance.

A. TERRAIN MAPPING

The procedure for terrain mapping includes raw measurement of bathymetry by underwater sonar sensors, outlier rejection in sonar profiles, and reconstruction of 3D point clouds of underwater terrains with the vehicle's pose information.

Several sonar sensors are available for bathymetry, including the single beam profiler, DVL, and MBES. For its superior efficiency, an MBES was selected in this work because it obtains hundreds of sonar ranges in a single scan, which

provides considerably more information than the other sonar ranging sensors. Bathymetry measurements by an MBES installed below a surface vehicle is illustrated in Fig. 1.

Sonar ranging has multipath propagation, generally caused by reflected sonar signals against water surfaces or the vehicle itself, and the sonar ranges affected by this should be corrected or rejected for consistent mapping. Assuming that the terrain captured in every sonar scan has a smooth and continuous shape and no high frequency components in a spatial domain, we can reject the outlier ranges using a threshold calculated as the average terrain height. The reconstruction is then achieved by converting inlier sonar ranges to the 3D point cloud of underwater terrain through coordinate transformation. Because the vehicle moves in a 3D space on the water surface, its pose state vector $\boldsymbol{\eta}$ can be described in an **SE**(3) group [25] by

$$\boldsymbol{\eta} = \begin{bmatrix} \boldsymbol{\eta}_1 \\ \boldsymbol{\eta}_2 \end{bmatrix} \tag{1}$$

where $\boldsymbol{\eta}_1 = [x, y, z]^\top$ is the 3D position of the vehicle, and $\boldsymbol{\eta}_2 = [\phi, \theta, \psi]^\top$ is the Euler angles describing the vehicle orientation, both represented in a global or inertial reference frame $\{\mathrm{I}\}$. We conveniently chose a universal transverse Mercator (UTM) coordinate system as an $\{\mathrm{I}\}$ frame, but any other global coordinate system can be selected depending on the application. Then, the conversion of the sonar ranges to terrain points can be formulated as

$$\boldsymbol{p}^{\mathrm{S}}_{k,t} = \begin{bmatrix} 0 \\ r_{k,t} \cos\left(\dfrac{\pi + s}{2} - kb\right) \\ r_{k,t} \sin\left(\dfrac{\pi + s}{2} - kb\right) \end{bmatrix} \tag{2}$$

where $r_{k,t}$ is the range measurement from the kth sonar beam at time step t, $\boldsymbol{p}^{\mathrm{S}}_{k,t}$ is the 3D point of terrain represented in a sonar sensor-fixed frame $\{\mathrm{S}\}$, s is the sonar scan width, and b is the beam spacing. $\boldsymbol{p}^{\mathrm{S}}_{k,t}$ is further converted to be represented in $\{\mathrm{I}\}$ by

$$\boldsymbol{p}^{\mathrm{I}}_{k,t} = \boldsymbol{R}^{\mathrm{I}}_{\mathrm{B}}(\boldsymbol{\eta}_{2,t})(\boldsymbol{R}^{\mathrm{B}}_{\mathrm{S}}\boldsymbol{p}^{\mathrm{S}}_{k,t} + \boldsymbol{t}^{\mathrm{B}}_{\mathrm{S}}) + \boldsymbol{\eta}_{1,t} \tag{3}$$

where $\boldsymbol{\eta}_{1,t}$ and $\boldsymbol{\eta}_{2,t}$ are the robot states at time step t, $R^{\mathrm{I}}_{\mathrm{B}}(\cdot)$ is a rotation matrix describing the transformation from $\{\mathrm{B}\}$ to $\{\mathrm{I}\}$, $R^{\mathrm{B}}_{\mathrm{S}}$ is a matrix describing the rotation from $\{\mathrm{S}\}$ to $\{\mathrm{B}\}$, and $\boldsymbol{t}^{\mathrm{B}}_{\mathrm{S}}$ is a translation vector describing the sensor position from the vehicle's motion center. The vehicle position $\boldsymbol{\eta}_{1,t}$ and orientation $\boldsymbol{\eta}_{2,t}$ can be measured using GPS and IMU, respectively.

Finally, the terrain map $\mathcal{T}$ consists of reconstructed 3D terrain points as follows:

$$\mathcal{T} = \{\boldsymbol{p}^{\mathrm{I}}_{k,t} | k = 1, \ldots, n_b, t = 1, \ldots, t_{\mathrm{s}}\} \tag{4}$$

where n_b is the number of sonar beams in a single scan, and t_{s} is the total time step taken for the sonar mapping.

B. GEOMAGNETIC FIELD MAPPING

The second type of geophysical property to be mapped is the geomagnetic field. The developed USV is equipped with high-precision underwater magnetometers and measures the 3D vector $\boldsymbol{m}^{\mathrm{M}}$ of the Earth's magnetic field in a magnetometer-fixed frame $\{\mathrm{M}\}$. However, magnetometers suffer from hard and soft iron effects caused by various electromagnetic devices and ferromagnetic materials, which bias the mapping results. Therefore, calibration of the magnetometers installed on the vehicle is an essential step for consistent mapping. We previously performed research in this area [20] and proposed a dedicated and efficient magnetic calibration method for USV applications. The same procedure was applied in this work, and the details are not described here. After calibration, the calibrated geomagnetic field measurements $\hat{\boldsymbol{m}}^{\mathrm{M}}$ compose an arc or circle of a unit sphere in a sensor-fixed frame. Then, they are transformed and represented in an $\{\mathrm{I}\}$ frame. The vehicle 3D orientation estimated by a gyroscope is used in this step. The conversion of the geomagnetic field values from the $\{\mathrm{M}\}$ to $\{\mathrm{I}\}$ frame is performed by

$$\boldsymbol{m}^{\mathrm{I}} = (R^{\mathrm{M}}_{\mathrm{I}})^{-1} \cdot \hat{\boldsymbol{m}}^{\mathrm{M}}. \tag{5}$$

The total strength of the geomagnetic field F is then calculated by

$$F = ||\boldsymbol{m}^{\mathrm{I}}||. \tag{6}$$

Because only a single 3D field vector is acquired along the vehicle's path, the resulting geomagnetic field strength map is quite sparse, and further interpolation is necessary to create a dense map, which is more useful for navigation than a sparse map. To this end, we employed Gaussian process regression (GPR) [26], a nonparametric regression method, and densified the sparse map. In GPR, the probability of the functions with two domains is defined as a normal distribution:

$$p(f(\boldsymbol{x}), f(\boldsymbol{x}')) = N(\boldsymbol{\mu}, \Sigma). \tag{7}$$

Here, the mean ($\boldsymbol{\mu}$) and covariance (Σ) of the functions are described by

$$\boldsymbol{\mu} = \begin{bmatrix} \mu(\boldsymbol{x}) \\ \mu(\boldsymbol{x}') \end{bmatrix}, \quad \Sigma = \begin{bmatrix} K(\boldsymbol{x}, \boldsymbol{x}) + \sigma_n^2 I & K(\boldsymbol{x}, \boldsymbol{x}') \\ K(\boldsymbol{x}', \boldsymbol{x}) & K(\boldsymbol{x}', \boldsymbol{x}') \end{bmatrix} \tag{8}$$

where σ_n^2 is the variance of the Gaussian noise in function observations, and K is a kernel function designed according to the problems. In this work, we apply a relatively simple squared exponential kernel:

$$K(\boldsymbol{x}, \boldsymbol{x}') = \sigma_f^2 \exp\left(-\frac{||\boldsymbol{x} - \boldsymbol{x}'||^2}{2l^2}\right) + \sigma_n^2 \delta(\boldsymbol{x}, \boldsymbol{x}') \tag{9}$$

where $\delta(\cdot)$ is a Kronecker delta function, σ_f^2 is the signal variance, and l is the length scale. Assuming a zero mean for the prior (i.e., $\boldsymbol{\mu} = \boldsymbol{0}$), the regression is calculated by

$$\mathbb{E}(f') = K(\boldsymbol{x}', \boldsymbol{x})[K(\boldsymbol{x}, \boldsymbol{x})^{-1} + \sigma_n^2 I]\boldsymbol{y} \tag{10}$$

$$\mathrm{cov}(f') = K(\boldsymbol{x}', \boldsymbol{x}') - K(\boldsymbol{x}', \boldsymbol{x})[K(\boldsymbol{x}, \boldsymbol{x}) + \sigma_n^2 I]^{-1} K(\boldsymbol{x}, \boldsymbol{x}') \tag{11}$$

where $\mathbb{E}(f')$ and $\mathrm{cov}(f')$ are the mean and covariance of the target function $f(\boldsymbol{x}')$, respectively, and $\boldsymbol{y}$ is the noisy observations of $f(\boldsymbol{x})$. The final dense geomagnetic field map can then be defined as

$$\mathcal{M} = \{\mathbb{E}(f')|\boldsymbol{x}' = \boldsymbol{x}_1, \boldsymbol{x}_2, \ldots, \boldsymbol{x}_n\} \tag{12}$$

where $\boldsymbol{x}_1, \boldsymbol{x}_2, \ldots, \boldsymbol{x}_n$ is the number of user-defined 3D positions in an operation area at which the magnetic field is interpolated.

When using the geomagnetic field map for navigation, we assume that the USV operates on a similar level of water surface as in the mapping phase, and tidal differences are negligible. To resolve these restrictions, one can further perform the downward or upward continuation [27] using the acquired magnetic field data and compensate for the tidal effects. This approach requires high fidelity for the continuation process (particularly for downward continuation) and was beyond the scope of this research.

III. GEOPHYSICAL NAVIGATION

The particle filter used in this study follows a standard framework of sampling-importance resampling (SIR) [10]. It maintains a set of N pose hypotheses, that is, particles $P_t = \{\boldsymbol{\eta}_t^{(i)}|i = 1, \ldots, N\}$. This particle set realizes the posterior probabilities of the target state $\boldsymbol{\eta}_t$ by a set of weights $W_t = \{w_t^{(i)}|i = 1, \ldots, N\}$. Algorithm 1 describes the particle filtering algorithm used in this work. The process consists of three steps: motion update, weight update, and resampling. These steps are performed on the basis of the designed vehicle motion and sensor observation models, which are explained in detail in the following sections.

Algorithm 1 Particle Filter-Based GN

Require: N (particle size), $\tilde{N}_{\mathrm{eff}}$ (effective sample size threshold), $\boldsymbol{\eta}_0$ (initial pose), $\boldsymbol{u}_{0:T-1}$ (control input), $\boldsymbol{\alpha}$ (motion noise parameters), $\boldsymbol{r}_{1:T}$ (sonar range measurement), $\boldsymbol{m}_{1:T}$ (magnetic field measurement), σ_{r}^2 (sonar range noise covariance), σ_{s}^2 (smoothing noise covariance), σ_{m}^2 (magnetic field noise covariance), $\tilde{R}_z$ (terrain roughness threshold), $\mathcal{T}$ (terrain map), $\mathcal{M}$ (geomagnetic field map), $\mathcal{R}_{\mathrm{s}}$ (region of interest for sonars), $\mathcal{R}_{\mathrm{m}}$ (region of interest for magnetometers), $\mathcal{S}$ (parameters for sonar sensing)

Ensure: $\boldsymbol{\eta}_t$ (robot pose), $\{\boldsymbol{\eta}_t^{(i)}\}$ (set of particles), $\{w^{(i)}\}$ (set of particle weight)

$\{\boldsymbol{\eta}_0^{(i)}\} \leftarrow \boldsymbol{\eta}_0$
$\{w^{(i)}\} \leftarrow 1/N$
for $t = 1$ to T **do**
  $\{\boldsymbol{\eta}_t^{(i)}\} \leftarrow$ motion_update$(\{\boldsymbol{\eta}_{t-1}^{(i)}\}, \boldsymbol{u}_{t-1}, \boldsymbol{\alpha})$
  if new $\boldsymbol{r}_t$ available **then**
    $R_z \leftarrow$ roughness$(\boldsymbol{r}_t)$
    $\{\hat{\boldsymbol{r}}_t^{(i)}\} \leftarrow$ ray_casting$(\{\boldsymbol{\eta}_t^{(i)}\}, \mathcal{T}, \mathcal{R}_{\mathrm{s}}, \mathcal{S})$
    if $R_z > \tilde{R}_z$ **then**
      $\{w^{(i)}\} \leftarrow$ weight_update$(\{w^{(i)}\}, \boldsymbol{r}_t, \{\hat{\boldsymbol{r}}_t^{(i)}\}, \sigma_{\mathrm{r}})$
    else
      $\{w^{(i)}\} \leftarrow$ weight_update$(\{w^{(i)}\}, \boldsymbol{r}_t, \{\hat{\boldsymbol{r}}_t^{(i)}\}, \sigma_{\mathrm{s}})$
    end if
  end if
  if new $\boldsymbol{m}_t$ available **then**
    $\{\hat{\boldsymbol{m}}_t^{(i)}\} \leftarrow$ ray_casting$(\{\boldsymbol{\eta}_t^{(i)}\}, \mathcal{M}, \mathcal{R}_{\mathrm{m}})$
    $\{w^{(i)}\} \leftarrow$ weight_update$(\{w^{(i)}\}, \boldsymbol{m}_t, \{\hat{\boldsymbol{m}}_t^{(i)}\}, \sigma_{\mathrm{m}})$
  end if
  $N_{\mathrm{eff}} \leftarrow 1/\sum_{i=1}^{N}(w^{(i)})^2$
  if $N_{\mathrm{eff}} < \tilde{N}_{\mathrm{eff}}$ **and** $R_z > \tilde{R}_z$ **then**
    $\{\boldsymbol{\eta}_t^{(i)}\} \leftarrow$ resample$(\{\boldsymbol{\eta}_t^{(i)}\}, \{w^{(i)}\})$
    $\{w^{(i)}\} \leftarrow 1/N$
  end if
  $\boldsymbol{\eta}_t \leftarrow \sum_{i=1}^{N} w^{(i)} \cdot \boldsymbol{\eta}_t^{(i)}$
end for

A. MOTION UPDATE

In this step, particles are moved and dispersed according to the vehicle motion model. We employ a velocity motion model [28], which assumes that vehicle motion is controlled by two velocities, a forward linear velocity v_t and a yaw angular velocity ω_t. The motion sensors used in this study included a DVL and fiber optic gyroscope (FOG), which provide measurements of v_t and ω_t, respectively. This control input $\boldsymbol{u}_t = [v_t, \omega_t]^\top$ is applied to each particle in a probabilistic manner to realize the uncertainty in motion prediction. We first sample a control input and an additional heading perturbation term $\hat{\gamma}$ as follows:

$$\hat{v} = v_t + \mathcal{N}(0, \alpha_1 v_t^2 + \alpha_2 \omega_t^2) \tag{13}$$
$$\hat{\omega} = \omega_t + \mathcal{N}(0, \alpha_3 v_t^2 + \alpha_4 \omega_t^2) \tag{14}$$
$$\hat{\gamma} = \mathcal{N}(0, \alpha_5 v_t^2 + \alpha_6 \omega_t^2) \tag{15}$$

where $\mathcal{N}(0, \sigma)$ is a sampled value from a normal distribution with zero mean and standard deviation σ, and a set of parameters $\boldsymbol{\alpha} = [\alpha_1, \alpha_2, \ldots, \alpha_6]$ describes the motion noise. α_1 and α_2 introduce the extent to which the uncertainty in the measurement of linear velocity grows with current linear and angular velocity, respectively, and α_3 and α_4 similarly establish the uncertainty in angular velocity. The vehicle pose is then updated using the following equations:

$$\begin{aligned}\boldsymbol{\eta}_{t+1}^{(i)} &= \boldsymbol{\eta}_t^{(i)} + \Delta\boldsymbol{\eta}_t^{(i)} \\ &= \boldsymbol{\eta}_t^{(i)} + \begin{bmatrix} -\frac{\hat{v}}{\hat{\omega}}\sin(\psi_t^{(i)}) + \frac{\hat{v}}{\hat{\omega}}\sin(\psi_t^{(i)} + \hat{\omega}\Delta t) \\ \frac{\hat{v}}{\hat{\omega}}\cos(\psi_t^{(i)}) - \frac{\hat{v}}{\hat{\omega}}\cos(\psi_t^{(i)} + \hat{\omega}\Delta t) \\ \mathcal{N}(0, \sigma_z) \\ \hat{\omega}\Delta t + \hat{\gamma}\Delta t \end{bmatrix}\end{aligned} \tag{16}$$

where σ_z is the disturbance in the vehicle's z-direction motion due to waves.

B. WEIGHT UPDATE

In this step, the weight of each particle is updated according to the likelihood of the predicted measurements from each

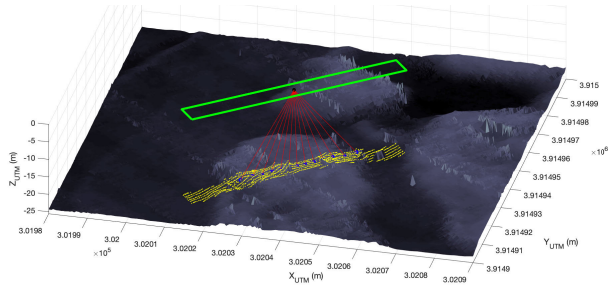

FIGURE 2. Observation of multibeam sonar range with ray casting.

particle given the actual sensor measurements. The predicted measurements are calculated from each sensor's observation models. For an MBES, two observation model types can be applied: projection-based and range-based [16]. In this work, we exploited the range-based model because it is more informative in the case of multibeam observations. Prediction of the sonar range is carried out by casting a ray in the beam direction and finding a hit point on the terrain map $\mathcal{T}$. Because the number of beams used in multibeam sonar sensing is several hundred, efficient ray casting is required. One basic approach is to downsample the beam measurements. Another approach is to reduce the map resolution. However, this has a limitation when the size of the target area is significantly large. Instead, we employed a region of interest (ROI) to restrain the search area for ray casting (Fig. 2). The ROI is set as a bounding box centered and oriented with the current pose with pre-defined width and height to cover the maximum roll and pitch of the vehicle. This approach greatly reduces the computational load and ensures scalability of the range-based observation model.

Once the range is predicted, the particle weight can be updated by

$$w_{\text{new}}^{(i)} = w_{\text{old}}^{(i)} \frac{1}{\sqrt{2\pi}\sigma_{\text{r}}} \exp\left[-\frac{1}{2\sigma_{\text{r}}^2}||\hat{\boldsymbol{r}}_t^{(i)} - \boldsymbol{r}_t||^2\right] \tag{17}$$

where $\boldsymbol{r}_t$ is the array of outlier-removed actual sonar ranges in a single scan at time step t, $\hat{\boldsymbol{r}}_t^{(i)}$ is the predicted sonar ranges from the i-th particle, and σ_{r}^2 is the noise covariance of the sonar range measurement. Here, the weight is updated in a productive fashion, but additive updates can also be used.

Similarly, the magnetometer measurement can be predicted by casting a single ray downward from the center of the magnetometer and finding a hit point on the magnetic field map $\mathcal{M}$. The particle weight update can be calculated by

$$w_{\text{new}}^{(i)} = w_{\text{old}}^{(i)} \frac{1}{\sqrt{2\pi}\sigma_{\text{m}}} \exp\left[-\frac{1}{2\sigma_{\text{m}}^2}||\hat{F}_t^{(i)} - F_t||^2\right] \tag{18}$$

where F_t is the actual geomagnetic field strength measured by a magnetometer at time step t, $\hat{F}_t^{(i)}$ is the predicted strength from the i-th particle, and σ_{m}^2 is the noise covariance of the magnetometer measurement.

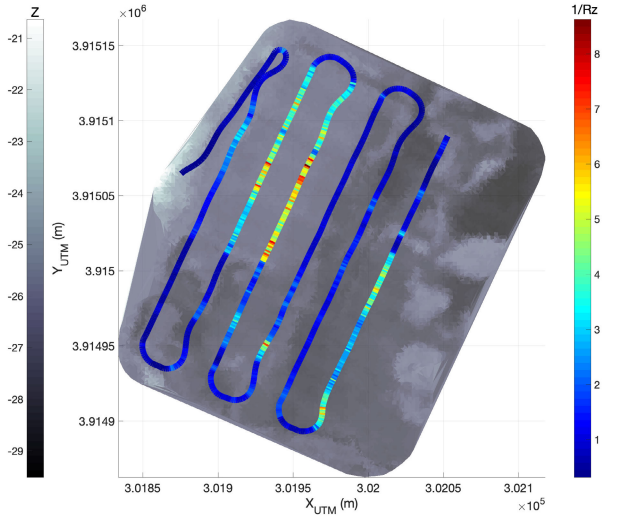

FIGURE 3. Terrain smoothness along the USV trajectory.

C. TERRAIN ADAPTIVE FILTER DESIGN

A conventional SIR filter has a particle impoverishment problem when the likelihood values between particles are highly similar over a certain span of time [17]. In our case, particle impoverishment can occur near the region where underwater terrain is flat. To resolve this problem, we employed a terrain roughness R_z and modified the weight update and resampling steps of the conventional filter based on the R_z values.

The R_z value for each sonar scan can be calculated by

$$R_z = \frac{1}{q}\Sigma_{i=1}^{q}(z_{\text{peak},i} - z_{\text{valley},i}) \tag{19}$$

where z_{peak} and z_{valley} are the values for the i-th highest peak and lowest valley, respectively, and q is the number of extreme z values used. This parameter represents the averaged maximum differences of terrain elevation captured in a single multibeam sonar scan. With a smaller R_z, the sensor covariance used in the weight update is selectively assigned with larger values. Then, (17) is modified as follows:

$$w_{\text{new}}^{(i)} = w_{\text{old}}^{(i)} \frac{1}{\sqrt{2\pi}\sigma_{\text{s}}} \exp\left[-\frac{1}{2\sigma_{\text{s}}^2}||\hat{\boldsymbol{r}}_t^{(i)} - \boldsymbol{r}_t||^2\right] \tag{20}$$

where σ_{s}^2 is the smoothed covariance of the sonar range measurement. The resampling step is also modified by restraining the resampling frequency for a small R_z. The modified steps are shown in lines 8–12 and 19–22 in Algorithm 1.

An example of the terrain smoothness ($1/R_z$) calculated along the vehicle trajectory is shown in Fig. 3 for the data obtained in our field test. The proposed filter adaptation method is applied to the area with $1/R_z$ larger than a certain threshold value (shown in yellow and red).

IV. FIELD TEST

A. EXPERIMENTAL SETUP

To verify the proposed GN method, a field test was performed in an inland water environment. The test site was the

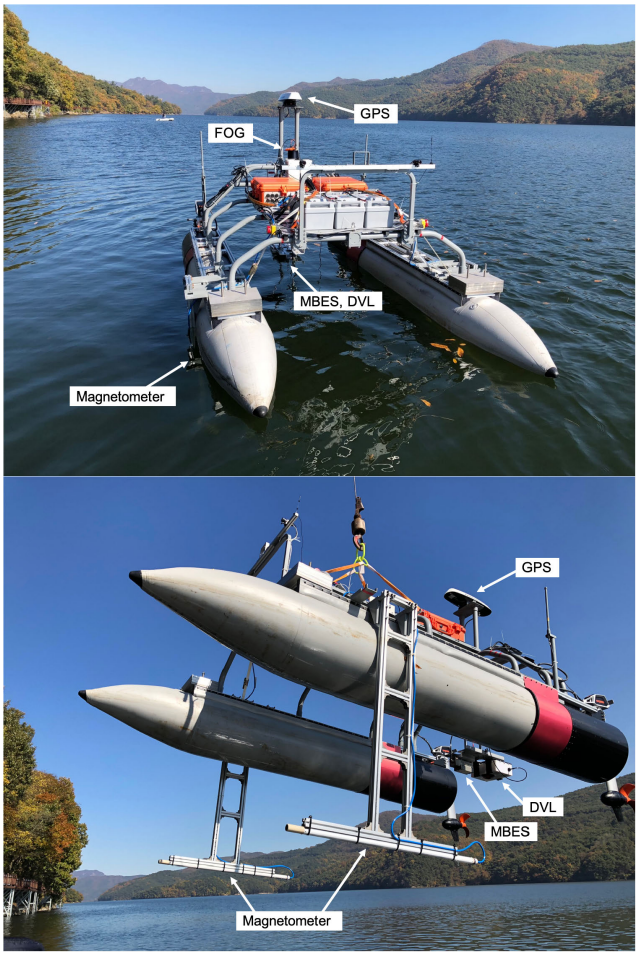

FIGURE 4. The USV developed at KRISO; equipped with INS sensors and geophysical sensors.

FIGURE 5. Planned USV trajectories for map construction (upper) and GN validation (lower).

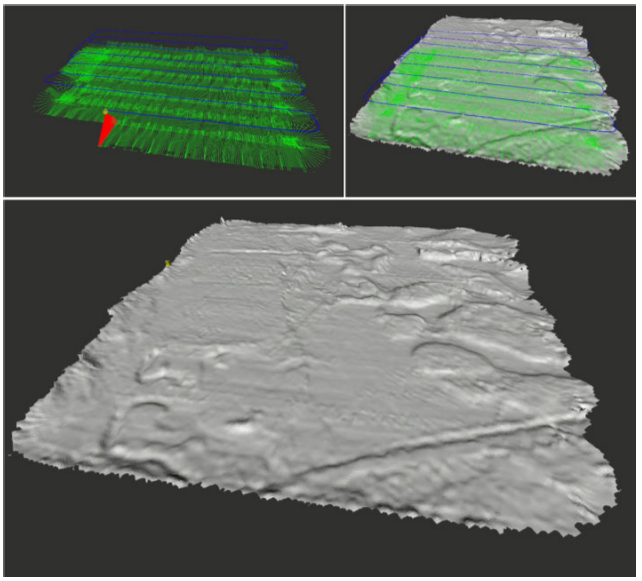

FIGURE 6. Constructed underwater terrain map. The vehicle trajectory (blue line) and MBES sonar scans (green dots) are shown.

Jang-Seong reservoir in South Korea, and a USV developed at KRISO (Fig. 4) was used for data acquisition. The vehicle was equipped with an Imagenex 837B MBES and a Bartington Grad-13S for sonar and magnetic sensing, respectively, and a Teledyne RDI Explorer DVL and Advanced Navigation Spatial FOG for DR. A Hemisphere GPS was used for geophysical map construction and reference path acquisition. All navigation algorithms were post-processed with MATLAB running on a 4.2 GHz Intel i7 PC with 32 GB RAM.

The USV autonomously followed two sets of trajectories, as shown in Fig. 5. One was used to construct a geophysical map over the test area, and the other was used to validate the navigation algorithms. The average speed of the vehicle was approximately 1.0 m/s, and approximately 1.5 h was consumed to obtain each data set.

B. MAPPING RESULTS

1) TERRAIN MAP

The constructed underwater terrain map from the first survey data is shown in Fig. 6. Approximately 16 million sonar ranges were processed to generate the terrain map. The size of the mapped area was approximately 200 m $\times$ 300 m. For the mapped area, the average depth of the reservoir was approximately 22 m. There are some distinct areas showing various heights, but most of the mapped areas are flat with few features. Before the reservoir was created by the dam, the area was a green field, which is why the underwater terrain is nearly flat. The original resolution of the map was approximately 0.1 m, and it was downsampled for computational efficiency when used in the navigation filter.

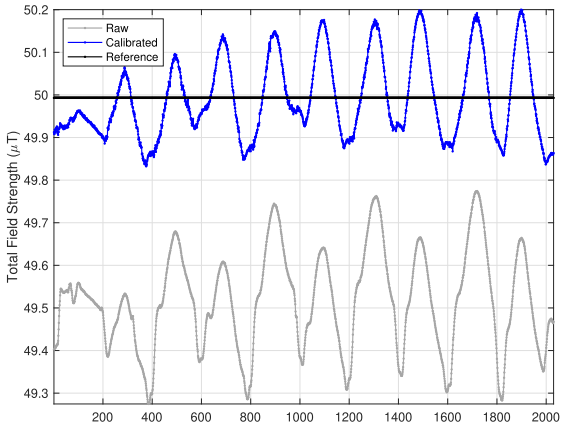

FIGURE 7. Magnetometer measurements and calibration results.

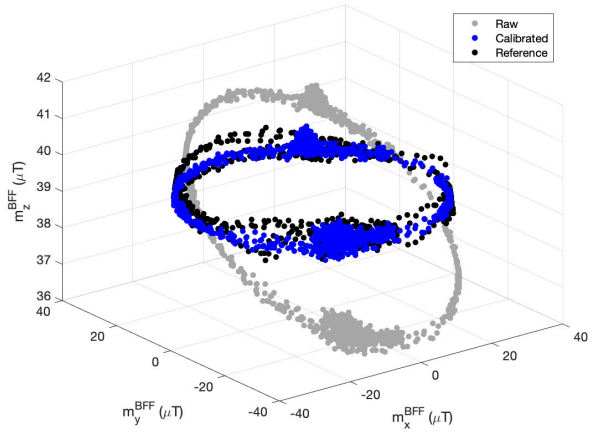

FIGURE 8. Scatter plot of magnetic field measurements represented in a sensor-fixed frame {M}.

2) MAGNETIC FIELD MAP

The geomagnetic field data obtained from the mapping procedure are shown in Fig. 7. The reference field strength (49.9931 μT) was employed from the recently published WMM data for the test site. Because the geomagnetic field in the test area has high strength in the center region (see Fig. 9) and the vehicle crossed the center region in a lawn-mower pattern, the sensor readings shown in Fig. 7 have repetitive convex and concave shapes. However, the raw magnetometer data set suffers from distortions and its convex peaks are not consistent, whereas the calibrated data show smooth peak amplitudes. The calibration results can be further verified from the scatter plot, as shown in Fig. 8. The 3D points of calibrated magnetic field measurements should consist of a horizontal circle when represented in the sensor-fixed frame. By applying the same calibration parameters to the magnetometer measurements in a navigation phase, we can exploit the geomagnetic field strength without bias. The final GPR-generated dense field map is shown in Fig. 9.

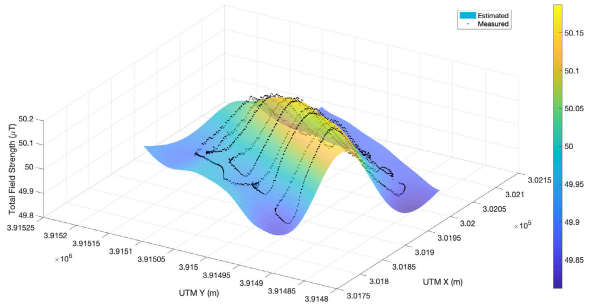

FIGURE 9. Interpolation of magnetic field map with GPR. Initial field strength measurements along with a vehicle trajectory are shown in black dots.

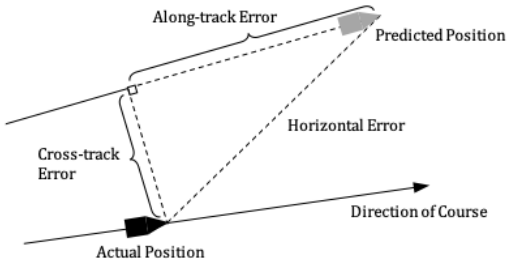

FIGURE 10. Illustration of tracking performance indices.

TABLE 1. Tracking performance (unit: m).

Method	Along-Track Error		Cross-Track Error	
	avg	std	avg	std
DVL-INS	8.13	3.55	4.32	3.08
TBN	3.86	4.28	3.84	5.40
MTBN	**3.32**	2.94	**2.30**	2.69
ATBN	**3.63**	2.93	**1.61**	1.84
MATBN	**3.73**	3.01	**1.56**	1.64

C. TRACKING RESULTS

Using the constructed geophysical maps described in the previous sections, we tested the performance of the proposed geophysical navigation method. For the GN filters, $N = 400$ was used for particle generation, and $\sigma_r = 0.85$ m and $\sigma_m = 0.1$ μT were set for the measurement models for the sonar and magnetometer, respectively. For the motion model, $\boldsymbol{\alpha} = [1.0, 10^{-4}, 10^{-2}, 10^{-4}, 10^{-4}, 10^{-4}]$ was used. For the adaptive filter, R_z and σ_s were set to $1/3$ and $10^2 \cdot \sigma_r$, respectively. All these parameters were selected empirically for our dataset to show the best performance for each tracking algorithm: 1) DVL-INS, 2) conventional TBN, 3) magnetic field-aided TBN (MTBN), 4) adaptive TBN (ATBN), and 5) magnetic field-aided adaptive TBN (MATBN). With this setup, for each algorithm we ran 100 Monte Carlo (MC) simulations and evaluated the tracking performance. The evaluation criteria we employed were along-track and cross-track errors, which are calculated as represented in Fig. 10.

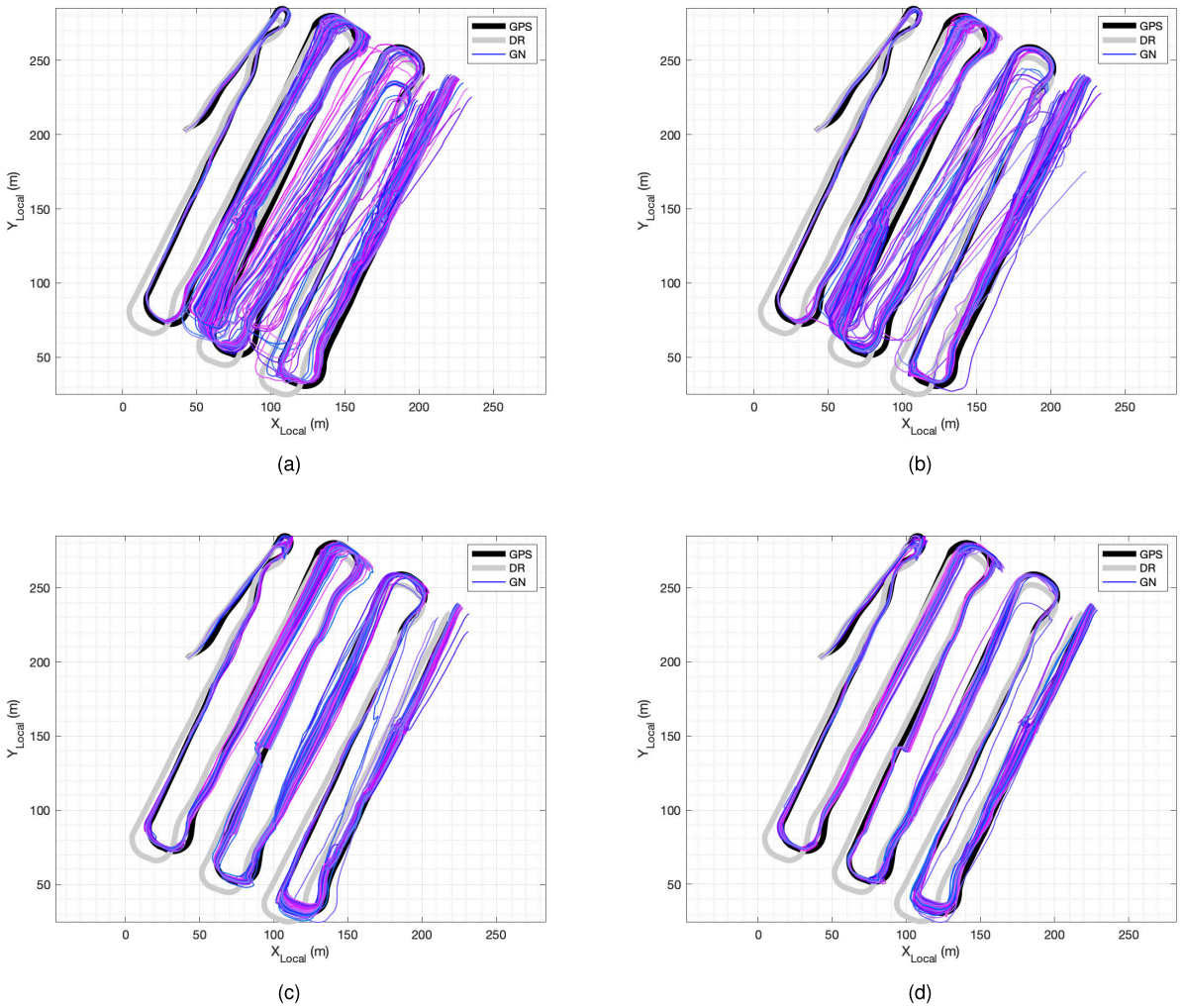

FIGURE 11. Tracking performance evaluated from 100 MC runs. Estimated trajectories from different GN methods are shown with reference (GPS) and DR (DVL-INS) paths. Applied GN methods were: (a) TBN, (b) MTBN, (c) ATBN, and (d) MATBN.

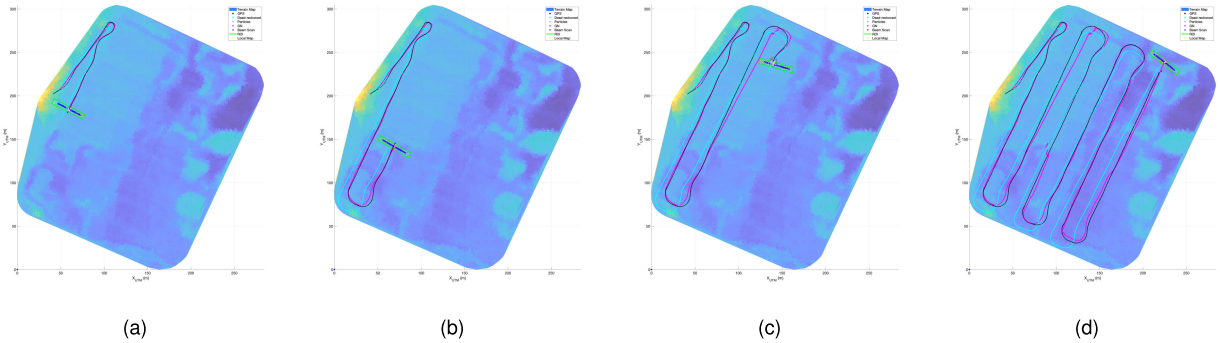

FIGURE 12. Example of ATBN tracking results. Reference path by GPS (black dots), DVL-INS estimation (cyan dots), and ATBN estimation (magenta dots); ROI for sonar observation (green box); and predicted sonar ranges (blue dots) are shown.

The tracking results of each algorithm are shown in Fig. 1 from the MC runs. The reference (GPS) and DVL-INS trajectories are shown in each plot for comparison. The accumulated error in DR is compensated by the conventional TBN when the terrain provides sufficient information in the initial segment of the trajectory (Fig. 11a). However, the conventional TBN fails in tracking when the vehicle approaches the area where the terrain roughness is low. This result is due to the local minima of filter estimation caused by particle impoverishment. In contrast, terrain adaptive TBN (Fig. 11c) alleviates this problem and shows significantly better performance, because the proposed filter adjusts both the

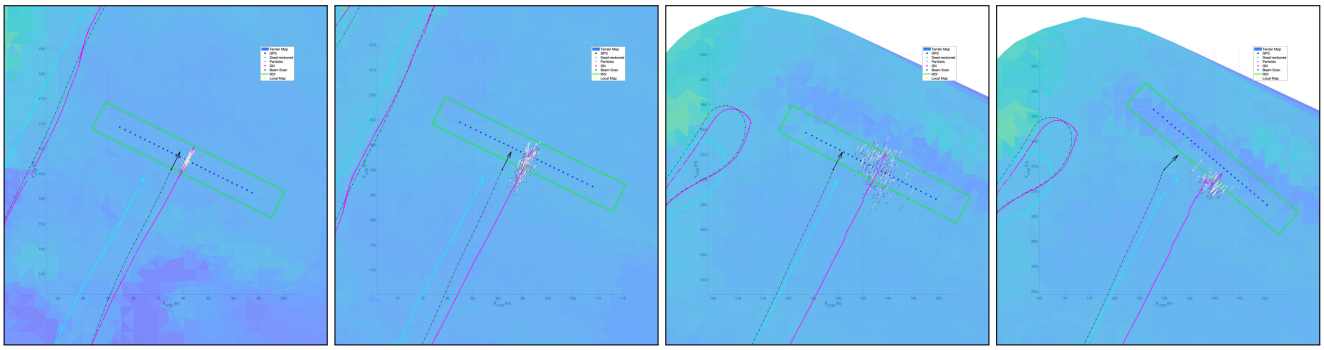

FIGURE 13. Detailed view of steps between Figs. 12b and 12c. The GN filter adjusts the weight update and resampling based on the terrain roughness. The particles (gray arrows) begin to spread when the vehicle passes over the uninformative region, and focus again as they encounter rough terrain.

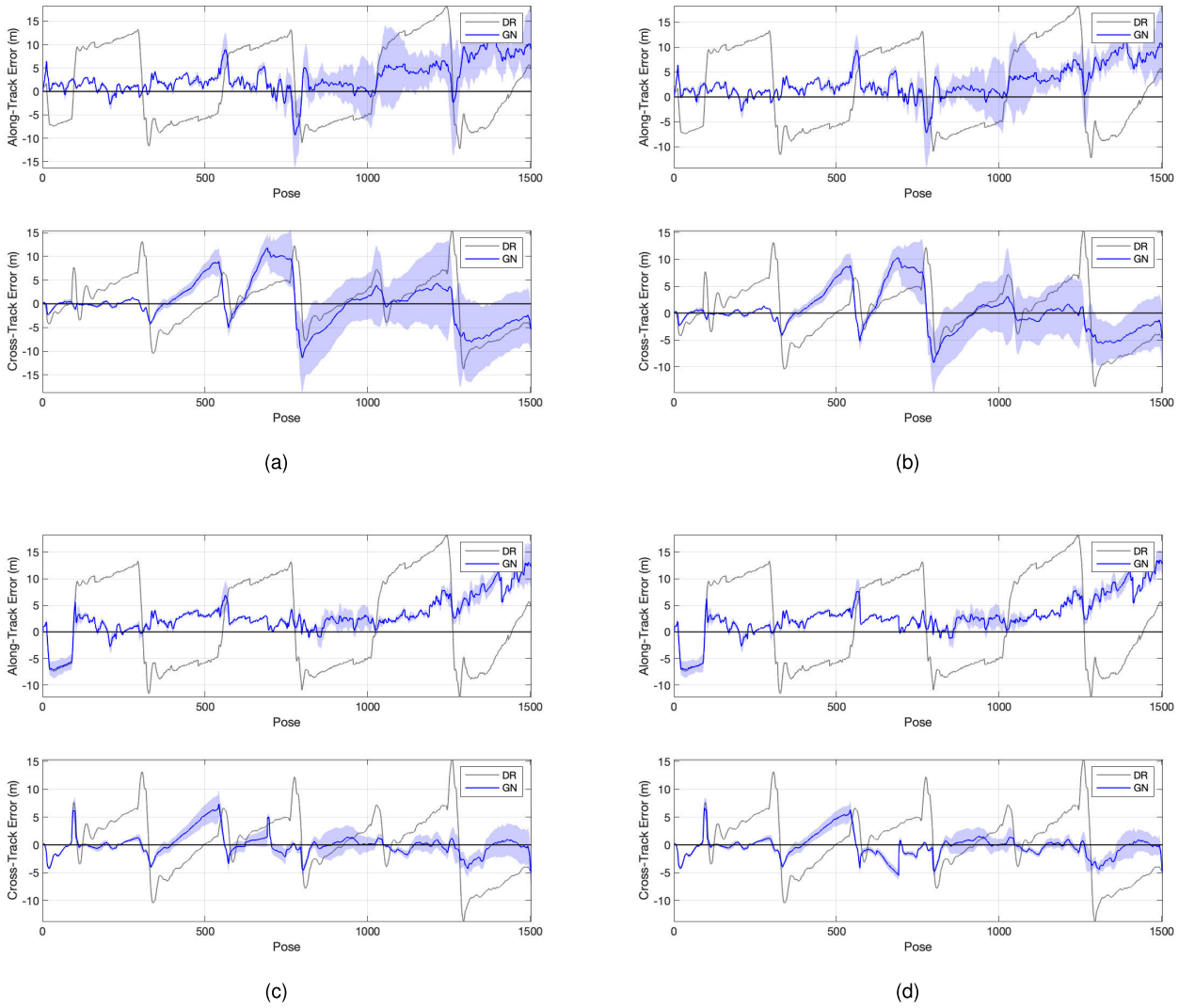

FIGURE 14. Evaluation of along-track and cross-track errors from 100 MC runs. The mean and standard deviation of errors for GN estimations are shown. (a) TBN, (b) MTBN, (c) ATBN, and (d) MATBN.

amount of the weight update and the frequency of resampling according to the usefulness of the terrain observations. This means that if sonar measurements are less informative, the filter tries to rely more on the motion update. The results of MTBN (Fig. 11b) and MATBN (Fig. 11d) compared with those of TBN and ATBN, respectively, validate that the

augmented observations by the magnetic field measurements further improve the tracking performances. The procedure of the adaptive GN is demonstrated in Figs. 12 and 13, where an instance of MC simulation for ATBN is shown.

The average tracking errors with standard deviations from 100 MC runs are shown in Fig. 14, and they are summarized in Table 1. The adaptive algorithms (ATBN and AMTBN) had slightly smaller along-track errors and considerably smaller cross-track errors compared with the TBN. The methods using magnetic fields (MTBN and MATBN) had smaller errors and deviations compared with the methods not using magnetic fields (except that the along-track errors of MATBN had slightly larger values).

V. CONCLUSION

In this study, we investigated a solution for USV navigation problems by exploiting underwater geophysical information. Two types of geophysical maps (underwater terrain and geomagnetic field strength maps) were constructed and utilized for navigation filters. We propose an improved version of TBN by applying a terrain adaptive particle filter implementation. In particular, we varied the resampling frequency and the amount of weight update according to the terrain roughness to address the particle impoverishment problems. As an additional geophysical property, geomagnetic field strength was augmented to the observation models. Experimental results validated the enhanced performance of the proposed GN methods compared with those of the DVL-INS and conventional TBN. We expect that exploiting more variable geomagnetic fields in other sites can lead to more drastic improvement of the tracking performances. The proposed GN methods can be employed for various civilian and military use cases where USVs are required to navigate under GNSS restrictions.

REFERENCES

[1] A. Grant, P. Williams, N. Ward, and S. Basker, "GPS jamming and the impact on maritime navigation," *J. Navigat.*, vol. 62, no. 2, pp. 173–187, Apr. 2009.
[2] N. O. Tippenhauer, C. Pöpper, K. B. Rasmussen, and S. Capkun, "On the requirements for successful GPS spoofing attacks," in *Proc. 18th ACM Conf. Comput. Commun. Secur.*, New York, NY, USA, 2011, pp. 75–86.
[3] T. Humphreys, B. Ledvina, M. Psiaki, B. O'Hanlon, and P. Kintner, "Assessing the Spoofing Threat: Development of a Portable GPS Civilian Spoofer," in *Proc. Inst. Navigat. GNSS (ION GNSS)*, 2008, pp. 2314–2325.
[4] *Enhanced Loran (Eloran) Definition Document*, document 1.0, 12, Jan. 2007.
[5] J. Oltmann and M. Hoppe, "Contribution to the IALA world wide radio navigation plan (IALAWWRNP)/recapitalization of MF DGNSS systems ENAV4-7.10A and ENAV4-7.10B," in *Proc. 4th IALA ENAV Committee Meeting*, 2008, pp. 1–6.
[6] G. W. Johnson, P. F. Swaszek, R. J. Hartnett, R. Shalaev, and M. Wiggins, "An evaluation of eLoran as a backup to GPS," in *Proc. IEEE Conf. Technol. Homeland Secur.*, Woburn, MA, USA, May 2007, pp. 95–100.
[7] G. W. Johnson, P. F. Swaszek, M. Hoppe, A. Grant, and J. Safar, "Initial results of MF-DGNSS R-Mode as an alternative position navigation and timing service," in *Proc. Int. Tech. Meeting Inst. Navigat.*, Monterey, CA, USA, Mar. 2017, pp. 1206–1226.
[8] J. Snyder, "Doppler velocity log (DVL) navigation for observation-class ROVs," in *Proc. OCEANS MTS/IEEE SEATTLE*, Seattle, WA, USA, Sep. 2010, pp. 1–9.
[9] H. C. Woithe, D. Boehm, and U. Kremer, "Improving slocum glider dead reckoning using a Doppler velocity log," in *Proc. OCEANS MTS/IEEE KONA*, Waikoloa, HI, USA, Sep. 2011, pp. 1–5.
[10] S. Thrun, W. Burgard, and D. Fox, *Probabilistic Robotics*. Cambridge, MA, USA: MIT Press, 2005.
[11] J. Han, J. Park, T. Kim, and J. Kim, "Precision navigation and mapping under bridges with an unmanned surface vehicle," *Auto. Robots*, vol. 38, no. 4, pp. 349–362, 2015.
[12] J. Han, J. Park, J. Kim, and N.-S. Son, "GPS-less coastal navigation using marine radar for USV operation," *IFAC-PapersOnLine*, vol. 49, no. 23, pp. 598–603, 2016.
[13] J. P. Golden, "Terrain contour matching (TERCOM): A cruise missile guidance aid," *SPIE*, vol. 238, pp. 10–18, Dec. 1980.
[14] S. Tuohy, N. Patrikalakis, J. Leonard, J. Bellingham, and C. Chryssostomidis, "AUV Navigation Using Geo-physical Maps with Uncertainty," in *Proc. 8th Int. Symp. Unmanned, Untethered Submersible Technol.*, 1993, pp. 265–276.
[15] J. Melo and A. Matos, "Survey on advances on terrain based navigation for autonomous underwater vehicles," *Ocean Eng.*, vol. 139, pp. 250–264, Jul. 2017.
[16] D. Meduna, "Terrain relative navigation for sensor-limited systems with application to underwater vehicles," Ph.D. dissertation, Dept. Aeronaut. Astronaut., Stanford Univ., Stanford, CA, USA, 2011.
[17] T. Li, S. Sun, T. P. Sattar, and J. M. Corchado, "Fight sample degeneracy and impoverishment in particle filters: A review of intelligent approaches," *Expert Syst. Appl.*, vol. 41, no. 8, pp. 3944–3954, Jun. 2014.
[18] J. F. Vasconcelos, G. Elkaim, C. Silvestre, P. Oliveira, and B. Cardeira, "Geometric approach to strap down magnetometer calibration in sensor frame," *IEEE Trans. Aerosp. Electron. Syst.*, vol. 47, no. 2, pp. 1293–1306, 2011.
[19] B. Allotta, R. Costanzi, F. Fanelli, N. Monni, and A. ridolfi, "Single axis FOG aided attitude estimation algorithm for mobile robots," *Mechatronics*, vol. 30, pp. 158–173, 2015.
[20] J. Jung, J. Park, J. Choi, and H.-T. Choi, "Autonomous mapping of underwater magnetic fields using a surface vehicle," *IEEE Access*, vol. 6, pp. 62552–62563, 2018.
[21] F. C. Teixeira and A. Pascoal, "Magnetic navigation and tracking of underwater vehicles," in *Proc. 9th IFAC Conf. Control Appl. Marine Syst. (CAMS)*, Osaka, Japan, 2013, pp. 239–244.
[22] *The GEBCO 2020 Grid—A Continuous Terrain Model of The Global Oceans and Land*, GEBCO Bathymetric Compilation Group 2020, National Oceanography Centre, Southampton, U.K., 2020.
[23] A. Chulliat, "The US/UK world magnetic model for 2015-2020," NOAA National Geophysical Data Center, Boulder, CO, USA, Tech. Rep., 2015, doi: 10.7289/V5TB14V7.
[24] E. Thébault, "International geomagnetic reference field: The eleventh generation," *Earth, Planets Space*, vol. 67, no. 79, pp. 1–19, 2015.
[25] T. I. Fossen, *Guidance and Control of Ocean Vehilcles*. Hoboken, NJ, USA: Wiley, 1994.
[26] C. E. Rasmussen and C. K. I. Williams, *Gaussian Processes for Machine Learning*. Cambridge, MA, USA: MIT Press, 2006.
[27] H. Schouten and K. McCamy, "Filtering marine magnetic anomalies," *J. Geophys. Res.*, vol. 77, no. 35, pp. 7089–7099, Dec. 1972.
[28] J. A. Fernandez-Madrigal, *Simultaneous Localization and Mapping for Mobile Robots: Introduction and Methods*. Hershey, PA, USA: IGI Global, 2012.

JONGDAE JUNG (Member, IEEE) received the B.S. degree in civil engineering from Hanyang University, Seoul, South Korea, in 2008, and the M.S. and Ph.D. degrees in civil and environmental engineering from the Korea Advanced Institute of Science and Technology (KAIST), Daejeon, South Korea, in 2010 and 2015, respectively. He is currently a Senior Researcher with the Korea Research Institute of Ships and Ocean Engineering (KRISO), Daejeon. His current research interests include intelligent maritime systems, multi-agent planning, and autonomous navigation of marine vehicles.

JEONGHONG PARK (Member, IEEE) received the B.S. and M.S. degrees in mechatronics engineering from Chungnam National University, Daejeon, South Korea, in 2005 and 2007, respectively, and the Ph.D. degree in mechanical engineering from the Korea Advanced Institute of Science and Technology (KAIST), Daejeon, in 2016. He is currently a Senior Researcher with the Korea Research Institute of Ships and Ocean Engineering (KRISO), Daejeon. His current research interests include ocean robotics, vision-based perception and tracking, and path planning of autonomous ships and marine robots.

JINWOO CHOI (Member, IEEE) received the B.S., M.S., and Ph.D. degrees in mechanical engineering from the Pohang University of Science and Technology (POSTECH), South Korea, in 2003, 2005, and 2011, respectively. He is currently a Senior Researcher with the Korea Research Institute of Ships and Ocean Engineering (KRISO), Daejeon, South Korea. His current research interests include mainly concentrated on mapping, localization, SLAM, and acoustic source localization for marine robots.

HYUN-TAEK CHOI (Member, IEEE) received the B.S., M.S., and Ph.D. degrees in electronic engineering from Hanyang University, Seoul, South Korea, in 1991, 1993, and 2000, respectively. He was an Associate Research Engineer with Korea Telecom, from 1993 to 1995. He was with the University of Hawaii, as a Postdoctoral Researcher, from 2000 to 2003. He is currently a Principal Researcher with the Korea Research Institute of Ships and Ocean Engineering (KRISO), Daejeon, South Korea. He has been leading several projects related to underwater robotic applications, such as design of ROVs and AUVs, advanced control and navigation, recognition using optic camera and sonar, and robot intelligence.